

Lower-Tropospheric Mixing as a Constraint on Cloud Feedback in a Multiparameter Multiphysics Ensemble

YOUICHI KAMAE

Faculty of Life and Environmental Sciences, University of Tsukuba, Tsukuba, Ibaraki, Japan, and Scripps Institution of Oceanography, University of California San Diego, La Jolla, California

HIDEO SHIOGAMA

Center for Global Environmental Research, National Institute for Environmental Studies, Tsukuba, Ibaraki, Japan

MASAHIRO WATANABE

Atmosphere and Ocean Research Institute, University of Tokyo, Kashiwa, Chiba, Japan

TOMOO OGURA AND TOKUTA YOKOHATA

Center for Global Environmental Research, National Institute for Environmental Studies, Tsukuba, Ibaraki, Japan

MASAHIDE KIMOTO

Atmosphere and Ocean Research Institute, University of Tokyo, Kashiwa, Chiba, Japan

(Manuscript received 3 January 2016, in final form 24 April 2016)

ABSTRACT

Factors and possible constraints to extremely large spread of effective climate sensitivity (ECS) ranging about 2.1–10.4 K are examined by using a large-member ensemble of quadrupling CO₂ experiments with an atmospheric general circulation model (AGCM). The ensemble, called the multiparameter multiphysics ensemble (MPMPE), consists of both parametric and structural uncertainties in parameterizations of cloud, cumulus convection, and turbulence based on two different versions of AGCM. The sum of the low- and middle-cloud shortwave feedback explains most of the ECS spread among the MPMPE members. For about half of the perturbed physics ensembles (PPEs) in the MPMPE, variation in lower-tropospheric mixing intensity (LTMI) corresponds well with the ECS variation, whereas it does not for the other half. In the latter PPEs, large spread in optically thick middle-cloud feedback over the equatorial ocean substantially affects the ECS, disrupting the LTMI–ECS relationship. Although observed LTMI can constrain uncertainty in the low-cloud feedback, total uncertainty of the ECS among the MPMPE cannot solely be explained by the LTMI, suggesting a limitation of single emergent constraint for the ECS.

1. Introduction

During these three decades, the uncertainty range of climate sensitivity (CS), determined as global-mean surface temperature increase in response to doubling of CO₂ concentration, has not been reduced efficiently (Knutti and Hegerl 2008; Maslin and Austin 2012)

despite improving quality of climate model projections (Reichler and Kim 2008). It is essential to achieve progress in understanding of factors contributing to the spread of CS and to constrain the spread from observational metrics with physical consistency (Fasullo et al. 2015; Klein and Hall 2015). Uncertainty in cloud feedback, the most important factor for the spread of CS (Dufresne and Bony 2008), has been examined by decomposing into different cloud properties including regionality, height, and optical depth (e.g., Zelinka et al. 2012a,b, 2013; hereafter Z13). For example, negative cloud feedback over the high latitudes associated with a

Corresponding author address: Youichi Kamae, Faculty of Life and Environmental Sciences, University of Tsukuba, 1-1-1 Tennoudai, Tsukuba, Ibaraki 305-8506, Japan.
E-mail: kamae.yoichi.fw@u.tsukuba.ac.jp

TABLE 1. List of models with n representing ensemble size. Old denotes that physics schemes of MIROC5 were replaced by those of MIROC3. MIROC5 convection scheme: prognostic closure with state-dependent entrainment (Chikira and Sugiyama 2010; Chikira 2010). Cloud scheme: prognostic cloud with mixed-phase microphysics (Watanabe et al. 2009; Wilson and Ballard 1999). Boundary layer scheme: Nakanishi–Niino–Mellor–Yamada level-2.5 closure (Nakanishi 2001; Nakanishi and Niino 2004). MIROC3 convection scheme: prognostic Arakawa–Schubert scheme with triggering function (Pan and Randall 1998; Emori et al. 2005). Cloud scheme: diagnostic cloud with simple microphysics (LeTreut and Li 1991; Ogura et al. 2008). Boundary layer scheme: Mellor–Yamada level-2.0 closure (Mellor and Yamada 1974, 1982). Check marks represent categories of the models.

	MIROC5A	Cld	Cnv	Vdf	CnvVdf	CldCnv	CldVdf	CldCnvVdf
n	20	20	20	11	12	20	15	18
Cloud scheme		Old				Old	Old	Old
Convection scheme			Old		Old	Old		Old
Boundary layer scheme				Old	Old		Old	Old
NewCnv	✓	✓		✓			✓	
OldCnv			✓		✓	✓		✓
MIROC3-like							✓	✓

phase change from ice to liquid cloud is physically consistent and robust among models (e.g., Tsushima et al. 2006; Zelinka et al. 2012b; Z13). In contrast, low cloud amount feedback over the ocean, the largest contributor to the total spread of cloud feedback (Bony and Dufresne 2005; Webb et al. 2006), still scatters substantially even in the state-of-the-art climate models [archived in phase 5 of the Coupled Model Intercomparison Project (CMIP5); Taylor et al. 2012] both in sign and magnitude (Vial et al. 2013; Z13; Qu et al. 2014).

The CMIP multimodel ensemble (MME) consists of general circulation models (GCMs) developed in different research groups but it does not necessarily cover the full range of possible uncertainty because similar model structures among some of them (e.g., Knutti et al. 2013) and limited ensemble members (Tebaldi and Knutti 2007; Collins et al. 2011). In previous literature, this sampling problem in “the ensemble of opportunity” was addressed using different experimental strategies. A well-known sampling strategy from perturbing parameters in model physics schemes [a perturbed physics ensemble (PPE)] is an effective way to examine dependencies of CS and climate feedbacks on model parameters in a given model structure (Murphy et al. 2004; Stainforth et al. 2005; Piani et al. 2005; Sanderson et al. 2010; Yokohata et al. 2010; Collins et al. 2011; Klocke et al. 2011; Shiogama et al. 2012; Webb et al. 2013; Yamazaki et al. 2013; Zhao 2014; Tomassini et al. 2015). Yokohata et al. (2010, 2013) and Sanderson (2011) compared PPEs based on different GCMs and revealed that parametric uncertainty depends on model structures; therefore, both structural and parametric uncertainties in CS should be examined in unified frameworks.

Structurally different GCMs can produce larger gaps of CS and cloud feedback than parametric uncertainty in a given model structure. Watanabe et al. (2012, hereafter W12) explored gaps of CS and cloud feedback

between different versions of MIROC climate model (section 2a) by using a multiphysics ensemble (MPE) developed by replacing physics schemes (cloud, cumulus convection, and turbulence) between the two GCMs (Table 1). Gettelman et al. (2012) also developed an MPE based on two versions of the Community Atmosphere Model. In addition, Shiogama et al. (2014, hereafter Shi14) developed PPEs based on the eight MPE models (W12), collectively called the multiparameter multiphysics ensemble (MPMPE), and examined the CS spread among it. The MPE consists of both low-CS and high-CS models (W12), resulting in an extremely wide range of CS (2.1–10.4 K) among the 136-member MPMPE. Cloud feedback, particularly shortwave (SW) radiation feedback over the ocean, is the dominant factor for the CS spread among the MPMPE, similar to the state-of-the-art MME. However, the largest contributors (low- or middle-cloud feedback over the tropical ocean) for the spreads of CS are suggested to be different among the eight PPEs with different model structures (Shi14). In Shi14, respective contributions from different types of cloud (cloud amount, height, and optical thickness; see section 2b) to the total spread in cloud feedback among the MPMPE were not explored. In addition, Shi14 examined cloud radiative feedback parameters simply by all-sky and clear-sky radiative balances (see section 2b), resulting in a possible artifact in the estimated cloud feedback due to noncloud effects.

By using above different types of ensembles (particularly MME and PPE), observational metrics (called emergent constraint) associated with cloud processes were applied to constrain the uncertainty range in CS (Fasullo et al. 2015; Klein and Hall 2015). Sherwood et al. (2014, hereafter She14) examined a possible correspondence between CS and intensity of vertical air mixing between the boundary layer and free

troposphere that is essential for the low cloud feedback (Brient and Bony 2013; Demoto et al. 2013; Zhang et al. 2013; Zhao 2014). Shi14 showed that the half of the CS variance among 43 CMIP3 and CMIP5 models can be explained by spread of lower-tropospheric mixing intensity (LTMI). As a result, the CS spread can be constrained by observed LTMI into higher value among the MME (>3 K). It is physically reasonable that GCMs with stronger low-latitude LTMI should be dryer in a warming climate, resulting in a stronger positive low-cloud feedback compared with weaker-LTMI GCMs (Fasullo et al. 2015; Klein and Hall 2015). However, correlation between LTMI and low-cloud feedback is not clearer than that for LTMI and CS, suggesting a remaining issue on physical consistency and effectiveness of LTMI for constraining the possible range of CS (Shi14; Klein and Hall 2015).

PPEs can be used as tests for physical consistency of the emergent constraint found in MMEs (Klein and Hall 2015). However, a PPE developed by a particular model structure is insufficient to examine a possible uncertainty range of CS. Therefore, we examine a physical consistency of LTMI to constrain spread of low-cloud feedback by using the large-member MPMPE. We examine respective roles of different types of cloud in the uncertainty in cloud feedback among the MPMPE by using satellite-simulator outputs (see section 2b). Results of this study reveal that LTMI can explain spread of low-cloud feedback but is not sufficient for constraint on CS uncertainty among the MPMPE. Section 2 describes data and methods used in this study. Section 3 explores general characteristics of cloud feedback among the MPMPE and decomposition of it into different cloud types. In section 4, roles of low- and middle-level cloud feedbacks in the CS spread are examined. Section 5 examines the relationships among LTMI, cloud feedback, and CS within the MPMPE. Section 6 provides a summary and discussion of this study.

2. Data and methods

a. Model and experiments

We use experimental data of MPMPE from Shi14, which is based on two versions of the atmospheric general circulation models (AGCMs): MIROC5 (hereafter MIROC5A; CS is 2.85 K; Watanabe et al. 2010) and MIROC3 (CS is 3.6 K; Hasumi and Emori 2004). First, MIROC5A and additional seven hybrid AGCMs together called the MPE (W12) were developed by replacing single or multiple physics schemes (cloud, cumulus convection, and turbulence) in MIROC5A to corresponding schemes adopted in MIROC3. For

example, the model in which convection scheme is replaced by that of MIROC3 is called Cnv (Table 1). See W12 for more details of MPE and numerical experiments. Second, Latin-hypercube sampling (McKay et al. 1979) was applied to the MPE models to develop eight PPEs (up to 20 members) by sweeping parameters for the cloud, cumulus convection, and turbulence schemes (Shi14). In total, 136 out of 20×8 members in the MPMPE (Table 1) are used in this study (remainders are not available due to numerical problems; see Shi14). Details of perturbed parameters in the physics schemes and their allowable ranges can be found in Table 2 of Shi14.

Next, 6-yr-long control (CTL) and two sensitivity experiments were conducted on 136 members in MPMPE to diagnose CS, forcing, and feedback. In CTL, AGCMs were forced by climatological sea surface temperature (SST) and sea ice from the preindustrial control simulation of the coupled atmosphere–ocean general circulation model (CGCM) version of MIROC5. CO_2 concentration was set to be identical to preindustrial run proposed in CMIP5 (273 ppmv). Next the increasing SST run and CO_2 run were performed by prescribing patterned SST increase and the quadrupling of CO_2 concentration, respectively. The prescribed SST increase and sea ice change were derived from the difference between the average of the years 11–20 from the CO_2 quadrupling run and the preindustrial run in the CGCM version of MIROC5. See Shi14 for more details of the experiments. From the three runs (CTL, SST, and CO_2), global-mean radiative forcing (RF), total radiative feedback parameter (λ), and effective CS (ECS) are determined as

$$\text{RF} = (R_{\text{CO}_2} - R_{\text{CTL}})/2, \quad (1)$$

$$\lambda = (R_{\text{SST}} - R_{\text{CTL}})/(\text{SAT}_{\text{SST}} - \text{SAT}_{\text{CTL}}), \quad \text{and} \quad (2)$$

$$\text{ECS} = -\text{RF}/\lambda, \quad (3)$$

where R represents global-mean radiative balance at the top of the atmosphere (TOA) and SAT denotes surface air temperature. Subscripts represent the names of the experiments. All the quantities are expressed as annual mean in this study. The factor of $1/2$ in Eq. (1) converts the RF of CO_2 quadrupling to that of doubling. Although a 6-yr integration would be short to estimate RF, λ , and ECS, the estimations are consistent with those derived from 20-yr integrations (Shi14). Note that the λ and ECS estimated in this method do not contain the nonlinear effect of λ (e.g., Armour et al. 2013; Andrews et al. 2015), suggesting a limitation for comparing with equilibrium CS obtained from long-term CGCM simulations (e.g., Andrews et al. 2012).

b. Diagnosing cloud radiative feedback parameters

Although some previous studies including Shi14 estimated cloud feedback by cloud radiative effect (difference between all-sky and clear-sky TOA radiation), such estimation could be biased due to contamination of noncloud radiative perturbation (e.g., Soden et al. 2008). In this study, cloud λ is diagnosed by using cloud radiative kernel method (Z13). The International Satellite Cloud Climatology Project (ISCCP) simulator (Klein and Jakob 1999; Webb et al. 2001) implemented in the MPMPE diagnoses cloud fraction at cloud-top pressure (CTP) ranges and cloud optical depth τ ranges in a similar manner to the satellite observation. The ISCCP simulator diagnoses 49 types of cloud ($7 \text{ CTP} \times 7 \tau$ bins) based on ISCCP cloud classification. Then simulator-produced clouds and ISCCP cloud radiative kernel are used to diagnose cloud λ . The radiative perturbation at TOA due to change in the simulated ISCCP clouds in the model can be diagnosed by multiplying radiative kernel [longwave (LW) and shortwave radiation components] and cloud fraction change in the 49 cloud bins. The sum of TOA radiative perturbation from all the 49 cloud bins per 1 K increase in global-mean SAT corresponds to total cloud λ . Net cloud λ (λ_{cld}) is derived from the sum of LW and SW cloud λ (λ_{LWcld} and λ_{SWcld}). In this study, we mainly focus on λ_{SWcld} because the contribution of λ_{SWcld} dominates the spread of ECS among the MPMPE (section 3a).

Here estimated cloud λ could be biased due to improper implementation of the ISCCP simulator. We tested consistency between total cloud fraction obtained from summing the CTP- τ histogram and total cloud fraction directly computed in the model cloud scheme (Zelinka et al. 2012a) and confirmed that the two show good agreements among MPMPE. The cloud λ can be decomposed into high, middle, and low CTP and thin, medium, and thick τ components by CTP and τ bins. In addition, we also utilize a partitioning method proposed in Z13 that can decompose the cloud λ into 1) cloud amount feedback, 2) CTP feedback, 3) τ feedback, and 4) a residual term. Cloud amount feedback represents a role of total cloud amount change in λ assuming a constant relative probability distribution in 49 types of ISCCP cloud. CTP (τ) feedback is derived by assuming constant τ (CTP) and total cloud amount. The ISCCP simulator and cloud radiative kernel can eliminate the noncloud radiative effect from the estimate of cloud λ (Z13).

c. Lower-tropospheric mixing intensity

In this study, the relationship between cloud radiative feedback parameters and LTMI among the MPMPE is

examined to explore generality of the relationship found in the MME (She14). LTMI consists of two components of lower-tropospheric mixing: small-scale mixing M_{small} via parameterized processes and large-scale mixing resolved in GCMs. Note that M_{small} is determined by a vertically integrated specific humidity tendency term (from 850 hPa to the surface) due to parameterized convection in GCMs averaged over the tropical ocean (30°S–30°N). She14 showed that drying of the boundary layer and moistening of the free troposphere via M_{small} and its change in a warming climate are stronger in higher-CS GCMs; the reverse is also true. However, most of GCMs did not provide the convective specific humidity tendency term to the CMIP5 archives. Therefore She14 proposed to use an index S calculated from resolved variables alternative to M_{small} . Differences of relative humidity (RH) and temperature (T) between the boundary layer (at 850 hPa) and free troposphere above the boundary layer (at 700 hPa) over the tropical deep convective region (the upper quartile of the annual-mean midtropospheric ascending motion; Fig. 1 in She14) are used to determine S . The differences of T ($\Delta T_{700-850}$; in kelvin) and RH ($\Delta \text{RH}_{700-850}$; in percent) are scaled; then S is derived as

$$S \equiv (\Delta \text{RH}_{700-850}/100 - \Delta T_{700-850}/9), \quad (4)$$

where 100% and 9 K are scaling factors to reduce the noise from other factors that affect $\Delta \text{RH}_{700-850}$ and $\Delta T_{700-850}$ (She14). Here the region used for calculating S is restricted to the tropical deep convective region to prevent contamination of nonlocal influence on humidity over the subsidence regions (She14). In this study, both M_{small} and S are examined.

As for the large-scale mixing, resolved vertical pressure velocity ω at the lower (700–850 hPa) and middle troposphere (400–600 hPa) are used (ω_1 and ω_2 , respectively). A ratio D (of shallow to deep overturning) and LTMI are determined as

$$D \equiv \langle \Delta H(\Delta) H(-\omega_1) \rangle / \langle -\omega_2 H(-\omega_2) \rangle \quad \text{and} \quad (5)$$

$$\text{LTMI} \equiv S + D, \quad (6)$$

where H is the step function, Δ is difference between ω_2 and ω_1 , and angle brackets indicate the areal average over the tropical ocean (30°S–30°N). Here She14 restricted the area for calculating D into 160°–30°E to avoid contamination of the effect of erroneously simulated shallow ascent over the warm ocean found in a few CMIP models. As for the MPMPE, simulated positions of the shallow ascent are similar (figure not shown) to the reanalyses (Fig. 3a in She14), resulting in a low sensitivity of results to choice of longitudinal area for calculating D .

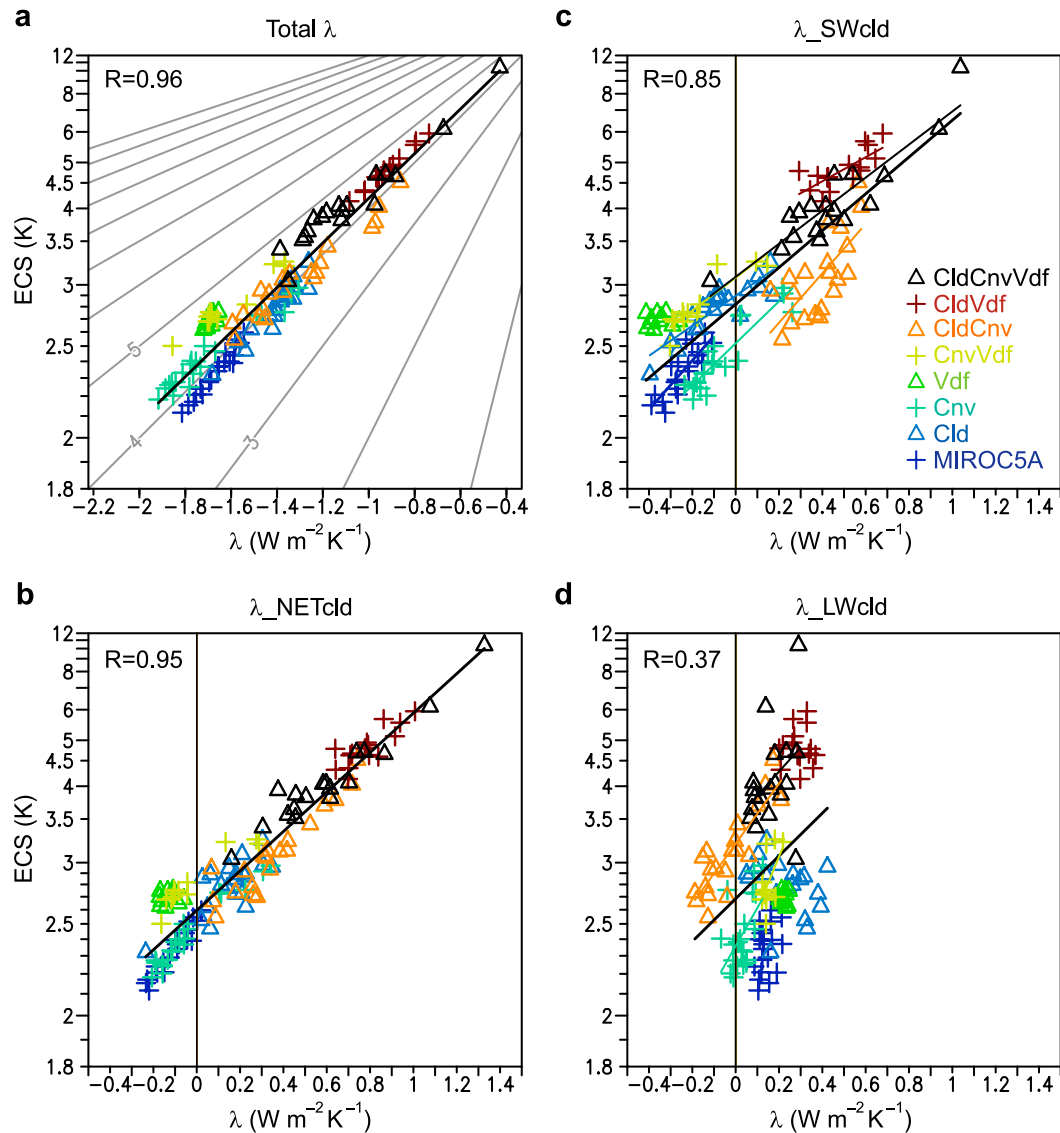


FIG. 1. Global-mean radiative feedback parameter (λ ; $\text{W m}^{-2} \text{K}^{-1}$) and ECS (K). (a) Scatterplot of total λ vs ECS among the MPMPE. Black lines indicate a least squares regression, and values plotted in the upper left the correlation coefficient. Plotted symbols and colors represent the eight PPEs based on individual MPPEs. Gray lines denote RF (W m^{-2}). Also shown are scatterplots of (b) λ_{cld} , (c) λ_{SWcld} , and (d) λ_{LWcld} vs ECS. Colored lines in (c),(d) denote least squares regressions of eight PPEs with statistical significance at the 90% level.

Observations and reanalyses data are used to obtain S , D , and LTM1 to constrain modeled λ and ECS in a similar manner to She14. The index S in observations and reanalyses is derived from She14 based on radiosonde observations [the Integrated Global Radiosonde Archive; see Sherwood et al. (2008) and She14] and gridded reanalyses data (ERA-Interim: Dee et al. 2011; and MERRA: Rienecker et al. 2011) averaged over the Indo-Pacific warm pool (Fig. 1 in She14). Observed D is derived from ω averaged over the tropical ocean in ERA-Interim and MERRA.

3. Forcing, feedback, and ECS in MPMPE

a. Total spread of ECS and cloud feedback among MPMPE

As a prelude to this study, we revisit the relationship of RF, λ , and ECS within the MPMPE. Figure 1a shows total λ and ECS among 136 members of the MPMPE. As shown in Shi14, total λ rather than RF determines the spread of ECS (92%) among the MPMPE (2.1–10.4 K) although RF also contributes partly to CS uncertainty among the MME (see Kamae et al. 2015, and

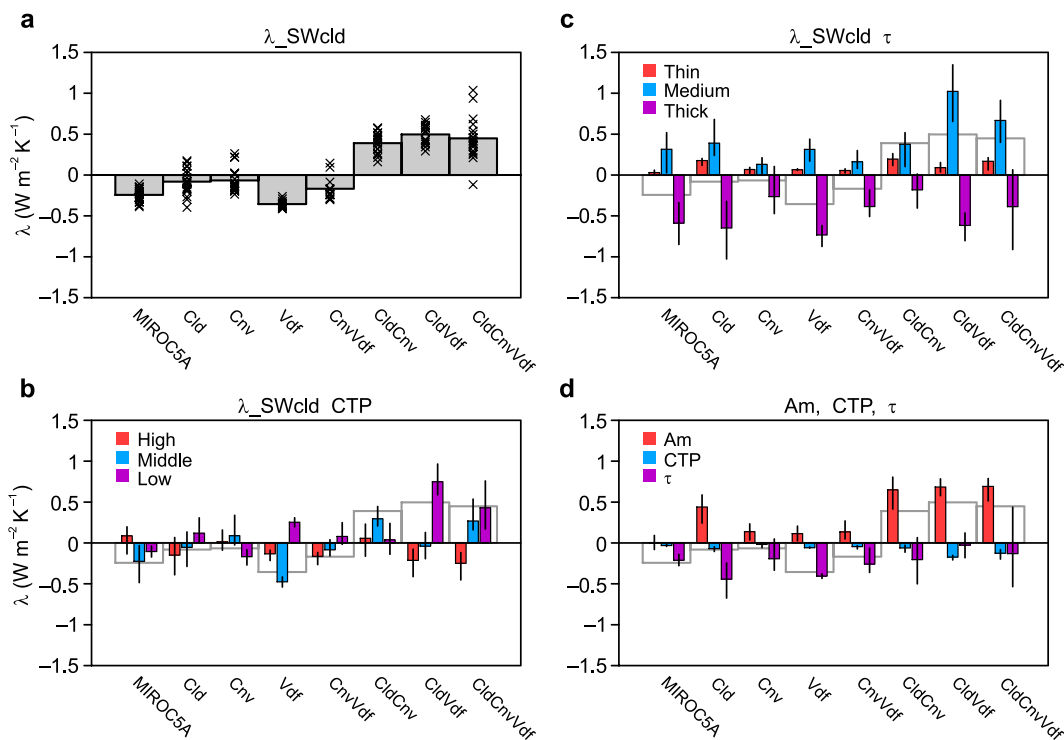


FIG. 2. Spread of λ_{SWcld} ($\text{W m}^{-2} \text{K}^{-1}$) and its decomposition. (a) Ensemble means of λ_{SWcld} in eight PPEs (bars) and individual ensemble members (crosses); (b) λ_{SWcld} decomposed into three CTP categories [high (50–440 hPa), middle (440–680 hPa), and low (680–1000 hPa)]. Error bars represent minimum-to-maximum ranges. Gray rectangles are identical to the bars in (a). (c) Decomposition into three τ categories [thin (0–3.6), medium (3.6–23), and thick (23–380)]. (d) Decomposition into cloud amount (Am), CTP, and τ feedback.

references therein). Here the vertical axis is scaled as $-1/\text{ECS}$ because ECS is in proportion to $-1/\lambda$, when RF ($3.6\text{--}4.7 \text{ W m}^{-2}$) is assumed to be constant [Eq. (3)]. Figures 1b–d show contributions of λ_{cld} , λ_{SWcld} , and λ_{LWcld} derived from the ISCCP simulator-produced cloud fraction and the cloud radiative kernel (section 2b). The term λ_{cld} also shows a high correlation with $-1/\text{ECS}$ ($R = 0.95$), suggesting a dominant contribution to the spread of ECS. Both the SW and LW radiation components contribute to the ECS spread but the former dominates (Figs. 1c,d). Figure 2a summarizes averages and individual members of λ_{SWcld} among PPEs. All the eight MPE models except Vdf show significant correlations between λ_{SWcld} and ECS (Fig. 1c), suggesting that both the differences among the MPE models and the spreads among the individual PPEs can largely be explained by λ_{SWcld} . Here the Vdf model has only 11 members (Table 1) because of numerical problems (Shi14), and the spread in λ_{SWcld} is smaller than the other models (Fig. 2a), resulting in an insignificant relationship between λ_{SWcld} and ECS (Fig. 1c). Note that the general characteristics of spreads and PPE-mean λ are consistent with Shi14

although they estimated the cloud feedbacks by using cloud radiative effect (section 2b).

Here the total spread of ECS and λ_{SWcld} among MPMPE consists both of structural uncertainty due to difference in model structure and parametric uncertainty associated with sensitivity on model parameters in a given model structure (see sections 1 and 2). In the next subsection, we focus on the structural uncertainty in λ_{SWcld} and then examine the parametric uncertainty in the eight PPEs.

b. Uncertainty in shortwave cloud feedback due to differences in model structure

As shown in W12 and Shi14, λ_{SWcld} in eight MPE models is diverse both in sign and magnitude (Fig. 2a), similar to CMIP5 MME (Vial et al. 2013; Z13). PPE-mean λ_{SWcld} values in five MPEs (MIROC5A, Cld, Cnv, Vdf, and CnvVdf) are negative whereas the others (CldCnv, CldVdf, and CldCnvVdf) are positive, contributing to the large ECS spread among the eight MPEs (W12; Figs. 1c and 2a). The differences associated with model structures are consistent with differences of ECS and λ_{SWcld} between MIROC5 and MIROC3 (Watanabe

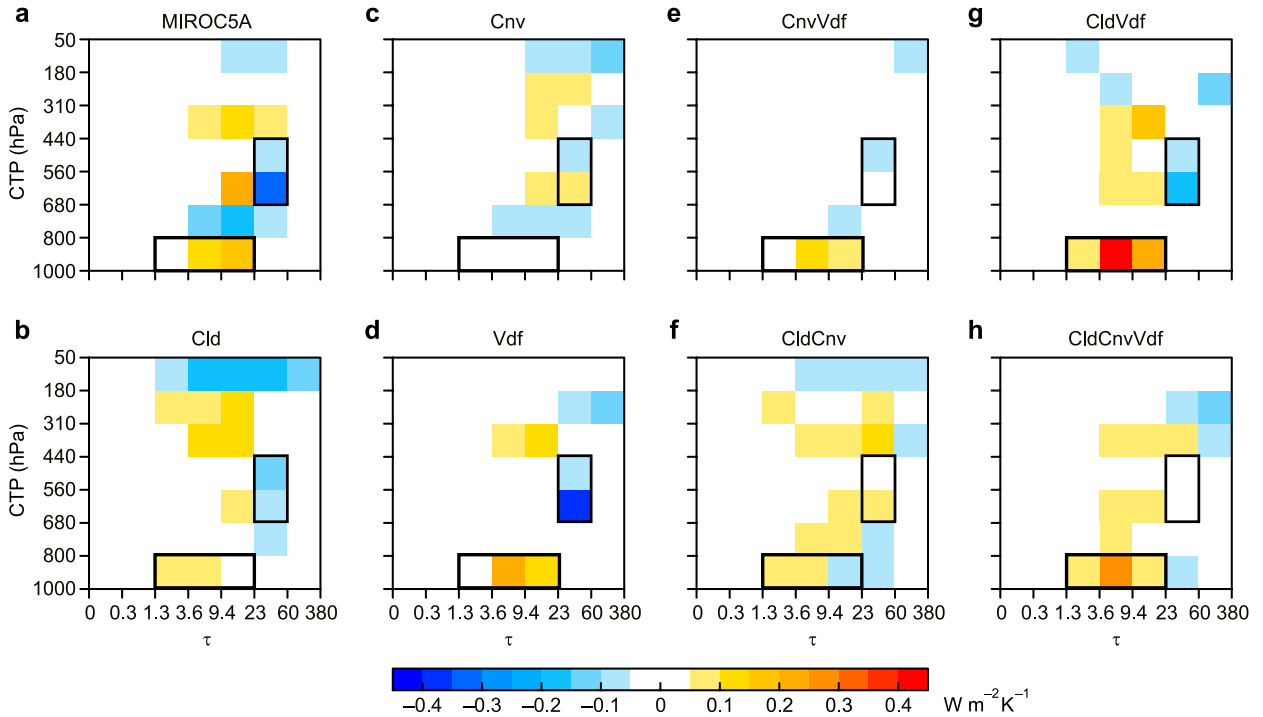


FIG. 3. The values of λ_{SWcld} ($\text{W m}^{-2} \text{K}^{-1}$) decomposed into 49 types of ISCCP clouds ($7 \text{ CTP} \times 7 \tau$ bins). Ensemble means of PPEs in (a) MIROC5A, (b) Cld, (c) Cnv, (d) Vdf, (e) CnvVdf, (f) CldCnv, (g) CldVdf, and (h) CldCnvVdf. Black rectangles represent cloud bins examined in sections 4 and 5.

et al. 2010; W12). The difference of λ_{SWcld} is further examined by decomposing into different types of cloud feedbacks. Figures 2b and 2c show the decomposition of λ_{SWcld} into different CTP and τ categories, respectively. Among the three categories of CTP [high (50–440 hPa), middle (440–680 hPa), and low (680–1000 hPa)], low and middle CTP mainly contribute to the difference of λ_{SWcld} among the eight MPEs. Low-CTP λ_{SWcld} is systematically negative in MIROC5A, while largely positive in CldVdf and CldCnvVdf (also called MIROC3-like models; Table 1). The difference of low-CTP λ_{SWcld} accounts for 0.85 (CldVdf minus MIROC5A) and 0.55 $\text{W m}^{-2} \text{K}^{-1}$ (CldCnvVdf minus MIROC5A), comparable to the differences in total λ_{SWcld} (Figs. 2a,b). However, the difference in middle-CTP λ_{SWcld} is also essential for large negative and positive λ_{SWcld} in Vdf and CldCnv, suggesting that a combination of the low- and middle-CTP λ_{SWcld} largely determines the inter-MPE variation (W12; Shi14).

The value of λ_{SWcld} decomposed into different τ categories (Fig. 2c) reveals that λ_{SWcld} due to the medium (thick) τ clouds is robustly positive (negative), consistent with CMIP5 MME (Z13). In a global warming simulations, τ increases substantially over the middle and high latitudes, resulting in a negative global-mean SW τ feedback (Zelinka et al. 2012b; Z13). Here inter-MPE

differences in medium and thick τ λ_{SWcld} contribute substantially to the spread among the MPEs despite the qualitative consistency (positive in medium and negative in thick categories) among them (Fig. 2c).

Figure 3 shows λ_{SWcld} divided into 49 bins based on seven CTP and seven τ bins. As shown in Fig. 2, contributions of inter-MPE spread in low-to-middle CTP (440–1000 hPa) and medium-to-thick τ clouds (3.6–380) dominate the total spread in λ_{SWcld} and ECS. Here some particular bin clouds strongly contribute to the total λ_{SWcld} spread. In MIROC5A, Cld, Vdf, and CldVdf, optically thick middle-top cloud (23–60 for τ and 440–680 hPa for CTP; black rectangles shown in Fig. 3) show large negative λ while the remainders show neutral or positive λ . This inter-MPE difference in these two bins can largely explain the difference in middle-top λ_{SWcld} shown in Fig. 2b. Spatial pattern and contribution to the total spread of ECS are examined in a later section. In addition, optically thin-to-medium low-top clouds (1.3–23 for τ and 800–1000 hPa for CTP; Fig. 3) also show substantial spread among the eight MPEs. The large λ_{SWcld} variation in these bins (neutral in Cnv and large positive in Vdf, CldVdf, and CldCnvVdf) largely corresponds to the inter-MPE variation of low-top λ_{SWcld} (Fig. 2b). It is interesting that low-ECS MIROC5A also shows positive λ_{SWcld} in 800–1000-hPa bins but large

negative λ_{SWcld} in 680–800-hPa bins and the optically thick middle-top cloud (Fig. 3a), resulting in a negative global-mean λ_{SWcld} (Fig. 2a).

Figure 2d shows the decomposition of λ_{SWcld} into cloud amount, CTP, and τ feedbacks among MPMPE. It is clearly shown that λ_{SWcld} due to cloud amount feedback dominates the total spread in λ_{SWcld} , suggesting that the total change in cloud amount rather shifts of probability density function in CTP– τ bins is important for the spread among the eight MPEs (Fig. 3). Here PPE-mean λ_{SWcld} due to cloud amount feedback is positive in all the eight MPEs, consistent with five CMIP5 models (Z13). It should be also noted that large negative λ_{SWcld} due to τ feedback also contribute to negative λ_{SWcld} in MIROC5A, Cld, Cnv, Vdf, and CnvVdf (Fig. 2d).

c. Parametric uncertainty in eight PPEs

As shown above, the inter-MPE variation in λ_{SWcld} substantially contributes to the ECS spread among the MPMPE. However, the large spreads of the ECS in the individual PPEs (except Vdf) apparently indicate an importance of parametric uncertainty in total spreads of λ_{SWcld} and ECS. For example, upper bounds of ECS (4.5, 5.9, and 10.4 K) and λ_{SWcld} are quite different among CldCnv, CldVdf, and CldCnvVdf (Figs. 1a,c) although PPE-mean λ_{SWcld} values are comparable (Fig. 2a). In addition, eight PPEs can provide systematic tests for robustness of different types of cloud feedback found among the MME (Vial et al. 2013; Z13). The parametric uncertainty and its dependency on the model structure are examined in this subsection.

The ranges of the parametric uncertainty are different among eight PPEs (Fig. 2a). MIROC5A and Vdf have relatively small spreads while CldCnvVdf has substantially large spread, contributing to the extremely high ECS members in CldCnvVdf (Fig. 1c). The large parametric uncertainty in low- and middle-top λ_{SWcld} (Fig. 2b) and medium- and thick- τ λ_{SWcld} (Fig. 2c) contributes to the large spread in total λ_{SWcld} , indicating that important contributors for intra-PPE spread also contribute to inter-PPEs spread. Figure 2d also reveals that both the intra-PPE and inter-PPE spreads in λ_{SWcld} due to cloud amount feedback are important for the total spread in λ_{SWcld} among the MPMPE. It should be noted that intra-PPE spread in λ_{SWcld} due to τ feedback is also predominant in some PPEs including CldCnvVdf (Fig. 2d). The extremely large spread of total λ_{SWcld} (Fig. 3a) in CldCnvVdf can be attributed to the spread of τ feedback (Fig. 2d). The λ_{SWcld} due to τ is consistently negative among CMIP5 MME (Z13) and most of the MPMPE (Fig. 2d) but largely positive in the extremely high ECS members of CldCnvVdf ($0.35\text{--}0.45\text{ W m}^{-2}\text{ K}^{-1}$).

Physical explanations and possible constraints on the positive λ_{SWcld} should be examined in future studies. However, the intra-PPE spread in λ_{SWcld} in CldCnvVdf corresponds well with LTMI (section 5).

The intra-PPE and inter-PPE spreads are comparable in low-top and middle-top clouds (Fig. 2). In the next section, we examine sources of uncertainty in λ_{SWcld} and ECS among all the MPMPE members including both the structural and parametric uncertainties.

4. Importance of middle and low cloud feedbacks for ECS spread

The results above reveal that both the spreads of low-top and middle-top cloud feedback show model-structure dependencies. Figure 4 shows spatial patterns of the first principal mode of interensemble variations in low-top (680–1000 hPa) and middle-top (440–680 hPa) cloud feedback among the MPMPE. These modes account for 39.2% and 45.8% of the variances in the low- and middle-top cloud feedback, respectively. Both of the first modes are dominant over the ocean, suggesting a limited contribution of land cloud feedback to the global-mean λ_{SWcld} spread (similar to CMIP5 MME; Vial et al. 2013; Kamae et al. 2016). In the low-top λ_{SWcld} , the large spread in the first mode is restricted to the subtropical–tropical ocean, similar to the inter-model variation in the low-top λ_{SWcld} among CMIP5 models (Fig. 8d in Vial et al. 2013). On the other hand, the large λ_{SWcld} in the first mode of the middle-top cloud is restricted to a narrow latitudinal band (Fig. 4c). These two leading modes are referred to as “oceanic low-cloud feedback” and “equatorial middle-cloud feedback” in this study. These two feedback components can explain a large part of the ECS spread among the MPMPE (detailed below).

Scores of principal components (PCs) of both the feedbacks (Figs. 4b,d) show clear model-structure dependencies. The PC1 scores in the oceanic low-cloud feedback (Fig. 4b) are lower in MIROC5A and higher in the MIROC3-like models (Table 1), consistent with the model-structure dependency found in Fig. 2b. The PC1 score in the equatorial middle-cloud feedback (Fig. 4d) can clearly be divided into two subsets: negative in MIROC5A, Cld, Vdf, and CldVdf (NewCnv subset; Table 1) and positive in the remainders (OldCnv subset). This grouping is apparently consistent with Figs. 2b and 3 (section 3). In short, the positive oceanic low-top λ_{SWcld} is large if both old Cld and Vdf schemes are implemented while the new Cnv scheme contributes to the large negative equatorial middle-top λ_{SWcld} .

Figure 5 shows the difference in the 49-bin λ_{SWcld} between CldCnvVdf and MIROC5A, Cnv, and

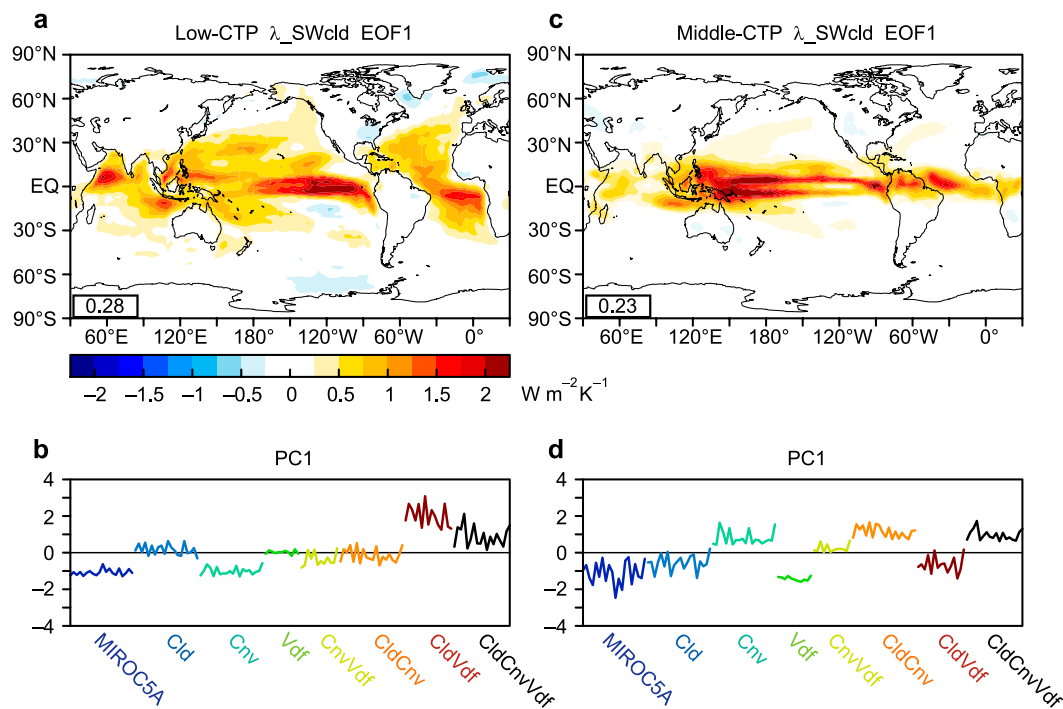


FIG. 4. PCs of λ_{SWcld} ($\text{W m}^{-2} \text{K}^{-1}$) variation among the MPMPE. (a) Spatial pattern of the first model of empirical orthogonal function in low-top λ_{SWcld} . Global mean is shown at the lower left in the panel. (b) PC1 scores for the individual members. (c),(d) As in (a),(b), but for middle-top λ_{SWcld} . These modes account for 39.2% and 45.8% of the variance in (a) and (c), respectively.

MIROC5A on the one hand and between CldVdf and MIROC5A on the other. Differences of spatial patterns of λ_{SWcld} in different CTP and τ categories are shown in Fig. 6. As suggested in section 3, the large difference of λ_{SWcld} between MIROC5A (low ECS) and CldCnvVdf (high ECS) can be found in the low-top bins and the optically thick middle-top bins (black rectangles in

Fig. 5). These two differences can be explained by the Cnv scheme and the combination of the Cld and Vdf schemes. Differences in λ_{SWcld} between Cnv and MIROC5A (CldVdf and MIROC5A) can be found in the optically thick middle-top (low-top) bins. Spatial patterns of the λ_{SWcld} difference (Fig. 6a) can also be approximated by the sum of the two (Figs. 6h,o),

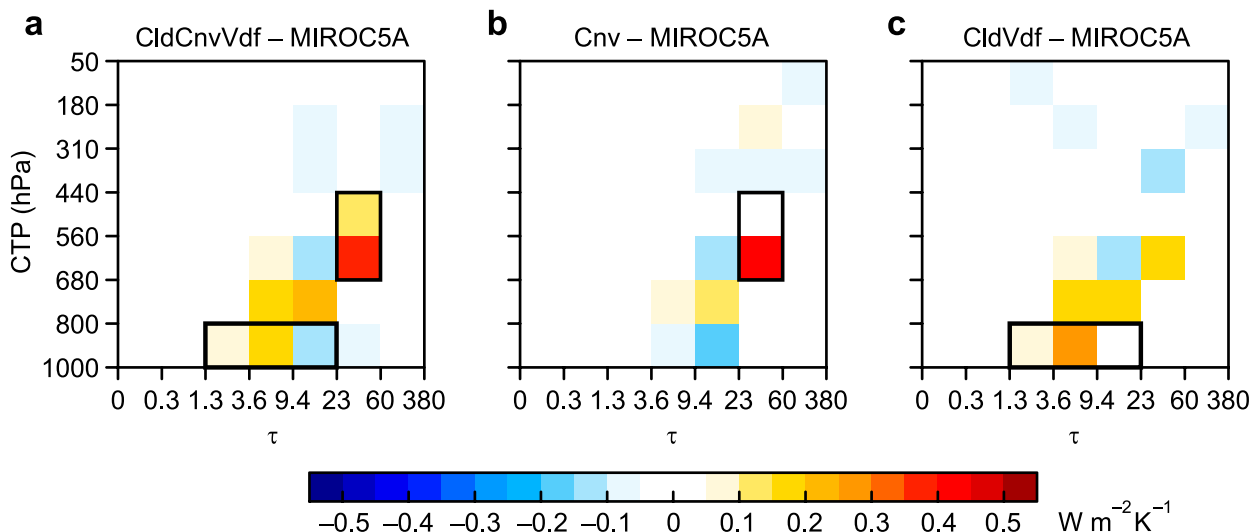


FIG. 5. As in Fig. 3, but for differences between (a) CldCnvVdf, (b) Cnv, and (c) CldVdf and MIROC5A.

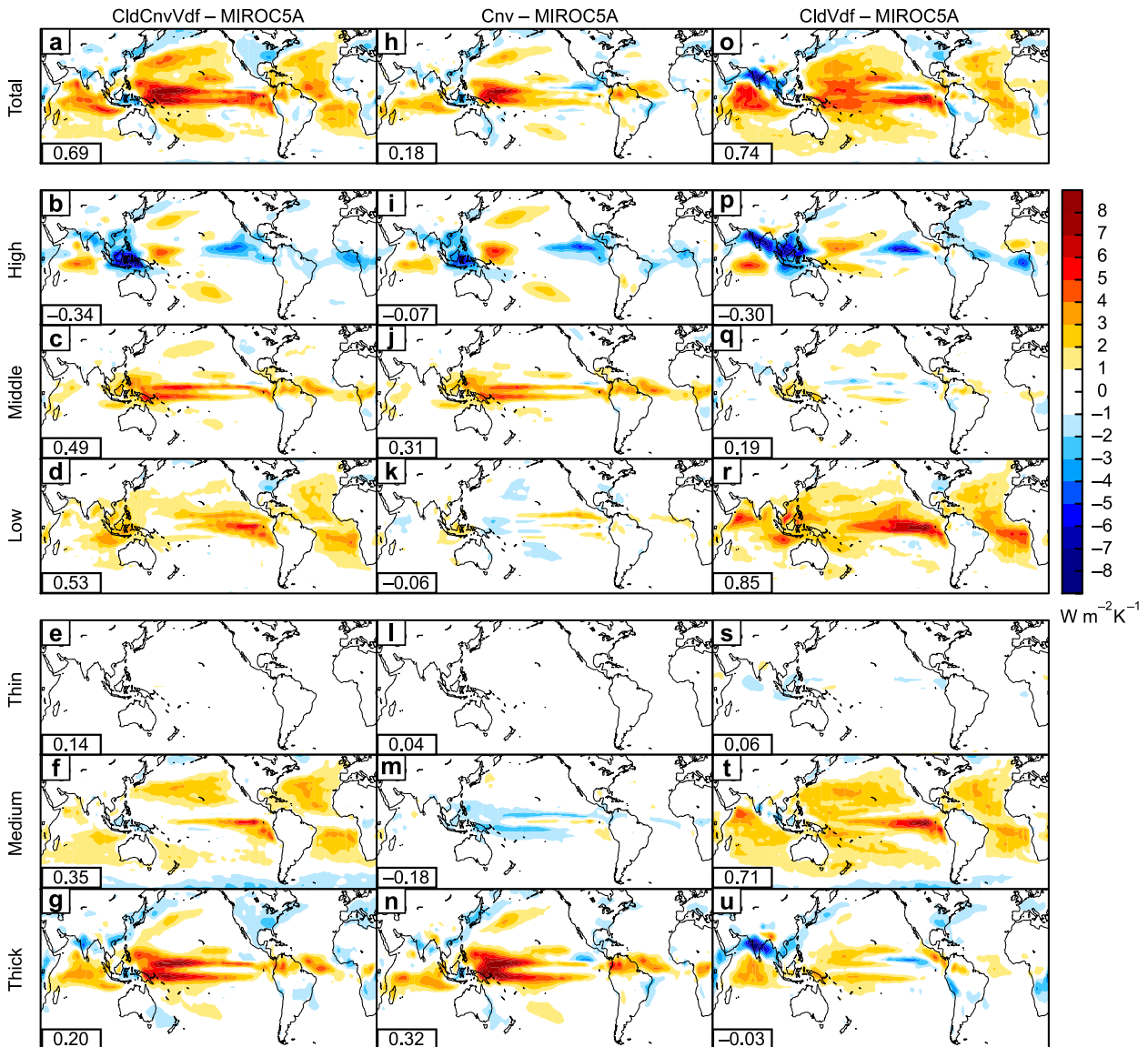


FIG. 6. Spatial patterns of λ_{SWcl} ($\text{W m}^{-2} \text{K}^{-1}$). (a) Difference between CldCnvVdf and MIROC5A. Also shown is the decomposition of (a) into (b) high-, (c) middle-, and (d) low-top clouds and into (e) thin, (f) medium, and (g) thick τ clouds. Global mean is shown at the lower left in each panel. (h)–(n) As in (a)–(g), but for Cnv minus MIROC5A. (o)–(u) As in (a)–(g), but for CldVdf minus MIROC5A.

consistent with the dominant modes among the MPMPE (Figs. 4a,c). The difference between Cnv and MIROC5A exhibits the equatorial middle-top λ_{SWcl} pattern (Figs. 6h,j), and is categorized into the optically thick cloud (Figs. 5b and 6n). A spatially similar pattern with reversed sign found in optically medium λ_{SWcl} (Fig. 6m) partly cancels this feedback. The difference between CldVdf and MIROC5A in the oceanic low-top λ_{SWcl} (Figs. 6o,r) dominates in the optically medium bin (Figs. 5c and 6t). The sum of these components can largely explain differences between CldCnvVdf and MIROC5A (Figs. 6a–g).

These two dominant modes of λ_{SWcl} can also explain intra-PPE variations of λ_{SWcl} and ECS. Figure 7 shows the relationship between λ_{SWcl} in the particular cloud bins (Fig. 5) and ECS among the MPMPE. In Fig. 7a, the optically thick middle-top (23–60 for τ and 440–680 hPa for CTP; Fig. 5) λ_{SWcl} explains intra-PPE variation in MIROC5A, Cld, and Vdf. The other four MPEs, with the exception of CldVdf, also show significant positive correlations (colored lines), suggesting the importance of the middle-top cloud feedback on the spread of ECS. The low-top (1.3–23 for τ and 800–1000 hPa for CTP; Fig. 5) λ_{SWcl} values show high correlations with ECS in high-ECS

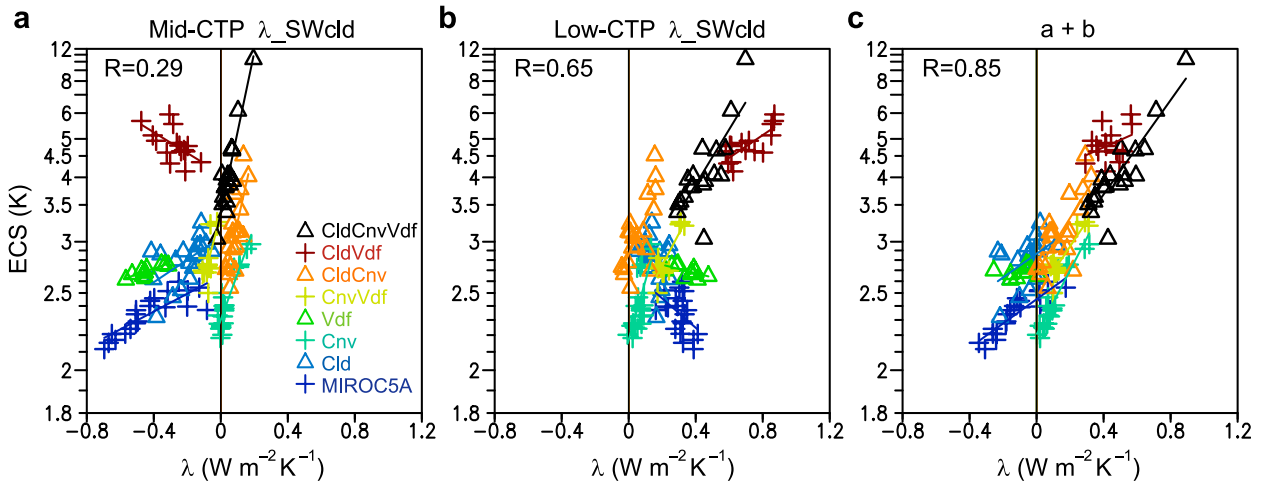


FIG. 7. As in Fig. 1c, but for λ_{SWcld} from particular cloud bins and ECS: (a) 23–60 for τ and 440–680 hPa for CTP (black rectangles in Fig. 3), (b) 1.3–23 for τ and 800–1000 hPa for CTP, and (c) sum of values from (a) and (b).

models (CnvVdf, CldCnv, CldVdf, and CldCnvVdf; Fig. 7b). In low-ECS MPEs, both positive (Cnv) and negative or insignificant (MIROC5A and Vdf) correlations are found (Fig. 7b). Interestingly, the sum of the two can explain 72% of the ECS variance among the MPMPE (Fig. 7c) despite their limited (5 out of 49) cloud bins. The results above (Figs. 2–7) indicate that the two components are effective to explain both the inter-PPE and the intra-PPE variations in λ_{SWcld} and the resultant ECS.

In MIROC5A PPE, ECS, and total λ_{SWcld} are largely determined by the equatorial optically thick middle-top λ_{SWcld} (Fig. 7a), consistent with previous studies [see Fig. 9 in Shiogama et al. (2012) and Fig. 3f in Shi14]. The strong middle-cloud feedback results in limited or negative correlation between the low-cloud λ and ECS (Fig. 7b; see also Fig. 3c in Shi14). In contrast, large parts of the ECS in the MIROC3-like PPEs are explained by the low-cloud λ over ocean [Figs. 4a and 7b; see also Fig. 6 in Yokohata et al. (2010) and Fig. 3 in Shi14]. As revealed in Yokohata et al. (2010), parametric uncertainty can be dependent on model structures, suggesting that single feedback processes such as low-cloud feedback cannot explain total ECS uncertainty among ensembles based on multiple model structures. In the remaining part of this paper, we examine possible applications of LTMI (section 1) for constraining λ_{SWcld} and ECS in the structurally different PPEs, namely the MPMPE.

5. Lower-tropospheric mixing intensity and cloud feedback

Figure 8 shows relationship between LTMI (and its components, S and D) and ECS among the MPMPE.

We divide the ensemble into two groups with old (OldCnv subset; section 4 and Table 1) and new convection schemes (NewCnv subset) because the LTMI–ECS relationships are clearly different between them. All the members of the OldCnv subset show clear positive correlations between S and LTMI (Fig. 8a), while none of the NewCnv subset do (Fig. 8b). Members in OldCnv subset with higher ECS clearly tend to have larger S although ECS scatters in a given S value (e.g., 2.3–3.1 K when $S = 0.36$). Positive correlations can also be found between D and ECS in the OldCnv subset with limited statistical significance (Fig. 8c) but are not found in the NewCnv subset (Fig. 8d). Resulting from the two, sum of S and D (=LTMI) corresponds well with ECS in all members of the OldCnv subset (Fig. 8e). The high correlations reveal that LTMI can explain the spread of ECS among half of the MPMPE subsets. Ranges of observed LTMI obtained from the reanalyses and radiosonde (section 2c) are comparable to that in the OldCnv subset. Here the upper end of the OldCnv subset is out of the observed range, suggesting that ECS values higher than 5.1 K are inconsistent with the observations. However, S , D , and LTMI do not show good correspondence with ECS among the NewCnv subset (Figs. 8b,d,f). Here LTMI–ECS correlations are significant (at 95% confidence level) among all the MPMPE members ($R = 0.67$) or the PPE-mean of the eight MPE models ($R = 0.71$; Fig. 9a). The positive correlation among the eight MPE models is consistent with the CMIP MME (She14) while their ranges and observation-based constraints are apparently different between the two (see section 6). Despite the significant positive correlations, intra-PPE correlations are negative in three PPEs (Fig. 8f), suggesting a limited

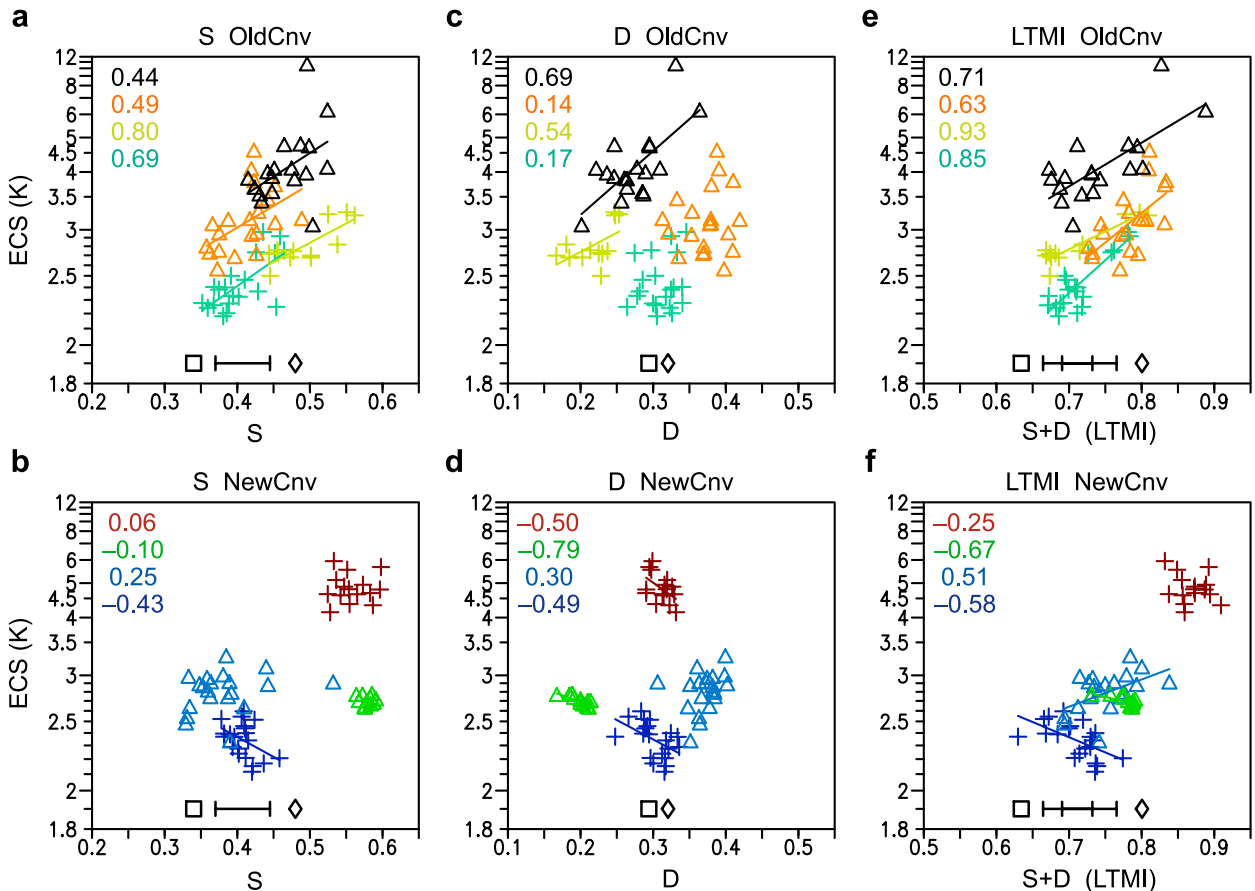


FIG. 8. Scatterplot of LTMI and ECS (K) among the MPMPE. Shown are (a) S , (c) D , and (e) LTMI ($=S + D$) and ECS among the OldCnv subset (Cnv, CldCnv, CnvVdf, and CldCnvVdf). (b), (d), (f) As in (a), (c), (e), but for the NewCnv subset (MIROC5A, Cld, Vdf, and CldVdf). Colored lines denote a least squares regression that is statistically significant at the 90% level (colors as in Fig. 7). Values at the top left show correlation coefficients of the individual PPEs. Black square and diamond across the bottom of each panel indicate S , D , and LTMI values derived from ERA-Interim and MERRA, respectively. Bars at the bottom in (a) and (b) represent 2σ range from radiosonde observation (She14). The two bars at the bottom in (e) and (f) denote the radiosonde added to D obtained from the reanalyses.

applicability of the LTMI-based constraint on ECS to the MPMPE.

We further examine why the constraint on ECS by LTMI is not effective for the NewCnv subset. Figure 10 shows the relationship between M_{small} (section 2c) and ECS among the MPMPE. She14 suggested that a larger M_{small} in a control climate results in a stronger drying of the boundary layer in a warming climate, resulting in a positive correlation between S and CS. Although M_{small} was only available from nine members in the CMIP MME (She14), M_{small} is available for all the MPMPE members. All members of the OldCnv subset show significant negative correlations between the two (Fig. 10a), supporting She14's results. In contrast, the NewCnv subset (except CldVdf) does not show significant negative correlations (Fig. 10b), consistent with the unclear S -ECS and LTMI-ECS relationships (Figs. 8b,f).

In the OldCnv subset, M_{small} explains well the spreads of low-top, middle-top (Fig. 10c,e), and total λ_{SWcld} (figure not shown), leading to the high M_{small} -ECS and LTMI-ECS correlations (Figs. 8e and 10a). A relationship between LTMI and low-top λ_{SWcld} shown in Fig. 9b and Table 2 is also statistically significant in the OldCnv subset, suggesting that the LTMI can constrain the low-top λ_{SWcld} . In the NewCnv subset, however, both M_{small} and the LTMI do not explain well the spread of ECS (Figs. 8f and 10b) despite significant negative correlations between M_{small} and low-top λ_{SWcld} (Fig. 10d) that are similar to the those in the OldCnv subset (Fig. 10c). Among all the MPMPE members, a lower range ($\leq 1.9 \text{ W m}^{-2} \text{ K}^{-1}$) of the low-top λ_{SWcld} is consistent with the observed LTMI (Fig. 9b). Note that two out of eight PPEs do not show significant positive correlations (Table 2).

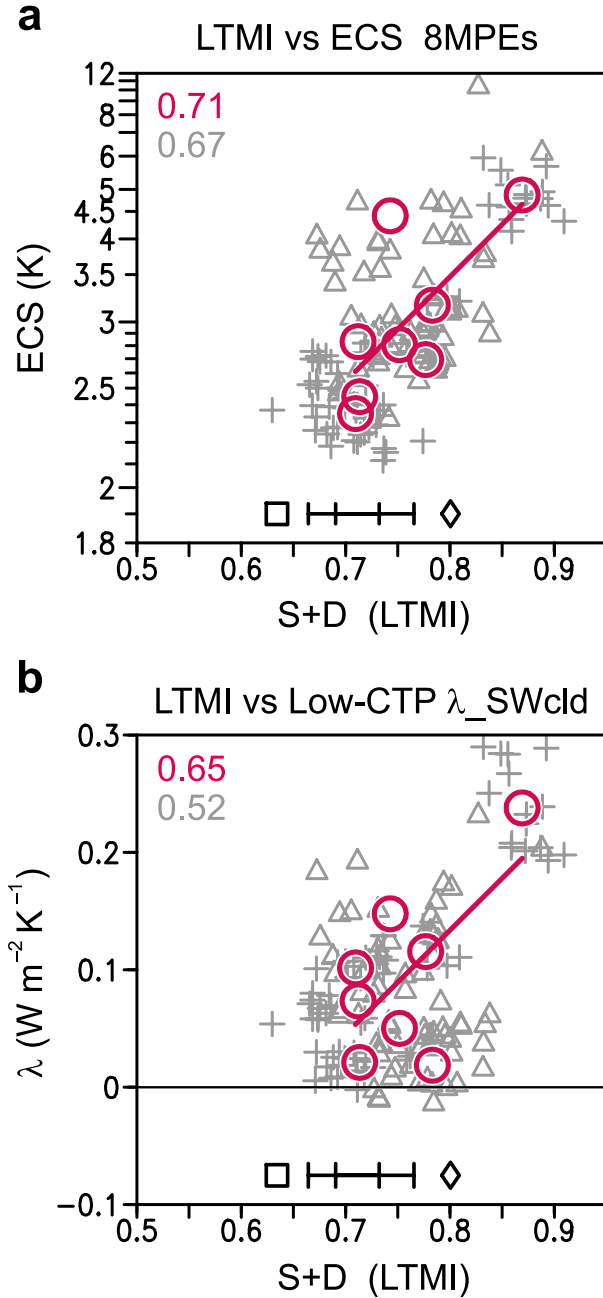


FIG. 9. (a) As in Figs. 8e,f, but for all the MPMPE members. Red circles and line represent PPE means of the eight MPE models and their least squares regression, respectively. Gray and red values at top left in the panels indicate correlation coefficients of all the MPMPE members and the PPE-means of the eight MPE models, respectively. (b) As in (a), but for a scatterplot of LTMI and λ_{SWcld} ($\text{W m}^{-2} \text{K}^{-1}$) in bins of 1.3–23 for τ and 800–1000 hPa for CTP (Fig. 7b).

The NewCnv subset has strong negative feedback in the equatorial middle-top cloud (Figs. 2–4 and 10f), resulting in the weak relationship between the low-top λ_{SWcld} and ECS (Fig. 7b). This is consistent with the

negative or insignificant M_{small} –ECS and LTMI–ECS correlations (Figs. 8f and 10b). Despite the high correlations among M_{small} , LTMI, and the low-top λ_{SWcld} (Figs. 9b and 10d), the large spread in the middle-top λ_{SWcld} (Fig. 10f) results in the unclear relationship between M_{small} (or LTMI) and total λ_{SWcld} (or ECS; Figs. 8f and 10b). It is noteworthy that significant correlations between M_{small} and the middle-top λ_{SWcld} are found both in the OldCnv and NewCnv subsets and these correlations are systematically opposite between the two (negative in the OldCnv subset and positive in the NewCnv subset; Figs. 10e,f). Physical processes responsible for the relationship between M_{small} (and LTMI) and the middle-top λ_{SWcld} should be examined in future studies.

6. Summary and discussion

The extremely large spread in ECS (2.1–10.4 K) found in the MPMPE is mainly due to the large structural and parametric uncertainty in λ_{SWcld} . Despite the qualitatively robust λ_{SWcld} components (positive thin- and medium- τ feedback, negative thick- τ feedback, positive amount feedback, and negative τ feedback), substantial spreads in the equatorial middle-top feedback and the oceanic low-top feedback contribute to the large spread in the total λ_{SWcld} both in sign and magnitude. Among the MPMPE, the NewCnv and the MIROC3-like subsets have large negative middle-top and positive low-top λ_{SWcld} , respectively. The sum of the two can explain 72% of the ECS spread among the MPMPE. ECS in the OldCnv subset largely depends on the low-top λ_{SWcld} , resulting in the high LTMI–ECS correlation because LTMI can explain the low-top λ_{SWcld} . In contrast, the high LTMI–ECS correlation cannot be found in the NewCnv subset. All the MPMPE members show high correlations between lower-tropospheric convective dehydration, a component of the LTMI, and the low-top λ_{SWcld} , supporting the hypothesis that LTMI can constrain the low cloud feedback. Among the MPMPE, members with low-top λ_{SWcld} higher than $1.9 \text{ W m}^{-2} \text{K}^{-1}$ are not supported by the observed LTMI. However, the large spread in the middle-top λ_{SWcld} in the NewCnv subset results in the limited applicability of the LTMI-based ECS constraint to the MPMPE. A possible emergent constraint for the middle-cloud feedback is necessary for more effective constraint on structural and parametric uncertainties in CS.

She14 concluded that CS is constrained to be higher than 3 K based on the observed LTMI and LTMI–CS relationship among the CMIP MME. This conclusion seems to be opposite to the current study (i.e., lower ECS members are more consistent with the observations

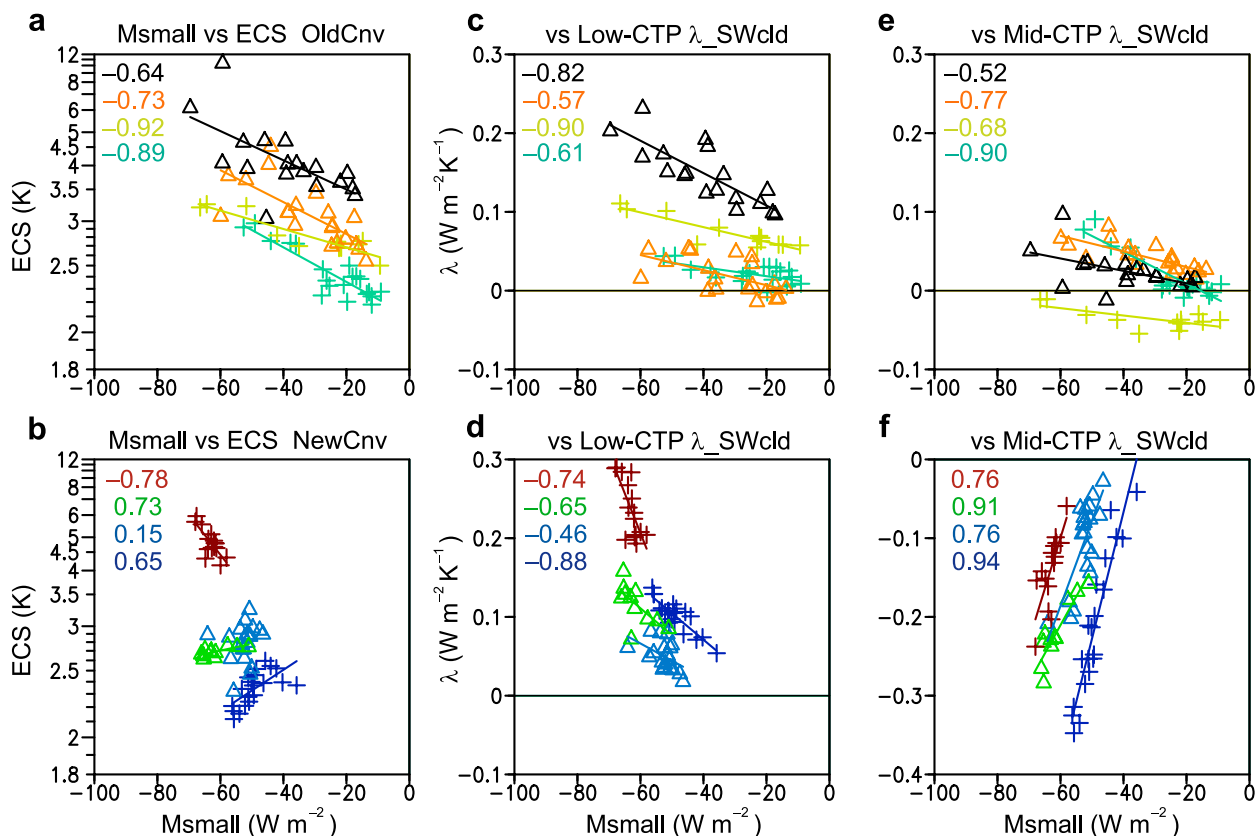


FIG. 10. (a) Scatterplot of M_{small} (W m^{-2}) and ECS (K) for the OldCnv subset. Values at top left in the panels indicate correlation coefficients of the individual PPEs; (c) M_{small} and λ_{SWcld} ($\text{W m}^{-2} \text{K}^{-1}$) in bins of 1.3–23 for τ and 800–1000 hPa for CTP (Fig. 7b); and (e) M_{small} and λ_{SWcld} in bins of 23–60 for τ and 440–680 hPa for CTP (Fig. 7a). (b), (d), (f) As in (a), (c), (e), but for the NewCnv subset.

than higher ECS members among the MPMPE). Both MIROC3 and MIROC5 models have relatively larger LTMI than the CMIP multimodel mean (Fig. 5b in She14), resulting in a less effective constraint of the lower ECS in the MPMPE (Fig. 9a). In addition, the CMIP MME does not cover the extremely high CS (Fig. 5b in She14), resulting in a difficulty for constraining the higher CS range. The difference in relative contributions of the middle-cloud feedback to the CS uncertainty is also one of the factors for the difference between the CMIP MME and the MPMPE.

The results of this study indicate that the relationship between LTMI and CS depends on ensembles. In CMIP3 and CMIP5 MME, intermodel variation of CS shows a high correlation with LTMI (She14) because the spread of low-cloud feedback is the largest contributor to the CS spread among the ensemble (Zelinka et al. 2012a; Z13; Vial et al. 2013). As for the NewCnv PPEs, the large uncertainty in the middle-top feedback results in the weak LTMI–ECS correlation. The convection scheme implemented in the NewCnv subset can represent the population of middle-level cumulus congestus

over the tropics realistically (Chikira and Sugiyama 2010; Chikira 2010). The large spread in the equatorial middle cloud feedback is associated with a model parameter in the cumulus scheme and extremely large negative feedback tends to be inconsistent with observed variables (Fig. 13 in Shiogama et al. 2012). It is worthwhile to note that multiple satellite observations should be used to evaluate cloud representations in models because of possible biases in the middle cloud observed by ISCCP and a limited accuracy of the

TABLE 2. Correlation coefficients between LTMI and λ_{SWcld} in bins of 1.3–23 for τ and 800–1000 hPa for CTP (Fig. 9b).

Models	Correlation coef
MIROC5A	0.56
Cld	0.85
Cnv	0.58
Vdf	0.55
CnvVdf	0.87
CldCnv	−0.28
CldVdf	0.45
CldCnvVdf	−0.52

simulator-produced clouds (e.g., Pincus et al. 2012). The results of this study suggest a need to evaluate representations of the tropical cumulus congestus both in MME and PPE and possible influence on the middle-top feedback and CS in systematic frameworks.

Acknowledgments. The authors thank M. Zelinka for providing the cloud radiative kernel. We appreciate J. D. Annan and J. C. Hargreaves for helpful discussion, and anonymous reviewers and S. A. Klein for their constructive comments. We acknowledge the scientific guidance of the World Climate Research Programme (WCRP) to promote this work, coordinated in the framework of WCRP Grand Challenge on Clouds, Circulation and Climate Sensitivity. This work was supported by the Program for Risk Information on Climate Change (SOUSEI program) of the Ministry of Education, Culture, Sports, Science and Technology (MEXT), Japan. The Earth Simulator at JAMSTEC and NEC SX at NIES were used to perform the model simulations.

REFERENCES

- Andrews, T., J. M. Gregory, M. J. Webb, and K. E. Taylor, 2012: Forcing, feedbacks and climate sensitivity in CMIP5 coupled atmosphere–ocean climate models. *Geophys. Res. Lett.*, **39**, L09712, doi:[10.1029/2012GL051607](https://doi.org/10.1029/2012GL051607).
- , —, and —, 2015: The dependence of radiative forcing and feedback on evolving patterns of surface temperature change in climate models. *J. Climate*, **28**, 1630–1648, doi:[10.1175/JCLI-D-14-00545.1](https://doi.org/10.1175/JCLI-D-14-00545.1).
- Armour, K. C., C. M. Bitz, and G. H. Roe, 2013: Time-varying climate sensitivity from regional feedbacks. *J. Climate*, **26**, 4518–4534, doi:[10.1175/JCLI-D-12-00544.1](https://doi.org/10.1175/JCLI-D-12-00544.1).
- Bony, S., and J. L. Dufresne, 2005: Marine boundary layer clouds at the heart of tropical cloud feedback uncertainties in climate models. *Geophys. Res. Lett.*, **32**, L20806, doi:[10.1029/2005GL023851](https://doi.org/10.1029/2005GL023851).
- Brient, F., and S. Bony, 2013: Interpretation of the positive low-cloud feedback predicted by a climate model under global warming. *Climate Dyn.*, **40**, 2415–2431, doi:[10.1007/s00382-011-1279-7](https://doi.org/10.1007/s00382-011-1279-7).
- Chikira, M., 2010: A cumulus parameterization with state-dependent entrainment rate. Part II: Impact on climatology in a general circulation model. *J. Atmos. Sci.*, **67**, 2194–2211, doi:[10.1175/2010JAS3317.1](https://doi.org/10.1175/2010JAS3317.1).
- , and M. Sugiyama, 2010: A cumulus parameterization with state-dependent entrainment rate. Part I: Description and sensitivity to temperature and humidity profiles. *J. Atmos. Sci.*, **67**, 2171–2193, doi:[10.1175/2010JAS3316.1](https://doi.org/10.1175/2010JAS3316.1).
- Collins, M., B. B. Booth, B. Bhaskaran, G. R. Harris, J. M. Murphy, D. M. Sexton, and M. J. Webb, 2011: Climate model errors, feedbacks and forcings: A comparison of perturbed physics and multi-model ensembles. *Climate Dyn.*, **36**, 1737–1766, doi:[10.1007/s00382-010-0808-0](https://doi.org/10.1007/s00382-010-0808-0).
- Dee, D. P., and Coauthors, 2011: The ERA-Interim reanalysis: Configuration and performance of the data assimilation system. *Quart. J. Roy. Meteor. Soc.*, **137**, 553–597, doi:[10.1002/qj.828](https://doi.org/10.1002/qj.828).
- Demoto, S., M. Watanabe, and Y. Kamae, 2013: Mechanism of tropical low-cloud response to surface warming using weather and climate simulations. *Geophys. Res. Lett.*, **40**, 2427–2432, doi:[10.1002/grl.50474](https://doi.org/10.1002/grl.50474).
- Dufresne, J.-L., and S. Bony, 2008: An assessment of the primary sources of spread of global warming estimates from coupled atmosphere–ocean models. *J. Climate*, **21**, 5135–5144, doi:[10.1175/2008JCLI2239.1](https://doi.org/10.1175/2008JCLI2239.1).
- Emori, S., A. Hasegawa, T. Suzuki, and K. Dairaku, 2005: Validation, parameterization dependence, and future projection of daily precipitation simulated with a high-resolution atmospheric GCM. *Geophys. Res. Lett.*, **32**, L06708, doi:[10.1029/2004GL022306](https://doi.org/10.1029/2004GL022306).
- Fasullo, J. T., B. M. Sanderson, and K. E. Trenberth, 2015: Recent progress in constraining climate sensitivity with model ensembles. *Curr. Climate Change Rep.*, **1**, 268–275, doi:[10.1007/s40641-015-0021-7](https://doi.org/10.1007/s40641-015-0021-7).
- Gottelman, A., J. E. Kay, and K. M. Shell, 2012: The evolution of climate sensitivity and climate feedbacks in the Community Atmosphere Model. *J. Climate*, **25**, 1453–1469, doi:[10.1175/JCLI-D-11-00197.1](https://doi.org/10.1175/JCLI-D-11-00197.1).
- Hasumi, H., and S. Emori, Eds., 2004: K-1 coupled model (MIROC) description. K-1 Tech. Rep., 34 pp. [Available online at http://ccsr.aori.u-tokyo.ac.jp/~hasumi/miroc_description.pdf.]
- Kamae, Y., M. Watanabe, T. Ogura, M. Yoshimori, and H. Shiogama, 2015: Rapid adjustments of cloud and hydrological cycle to increasing CO₂: A review. *Curr. Climate Change Rep.*, **1**, 103–113, doi:[10.1007/s40641-015-0007-5](https://doi.org/10.1007/s40641-015-0007-5).
- , T. Ogura, M. Watanabe, S.-P. Xie, and H. Ueda, 2016: Robust cloud feedback over tropical land in a warming climate. *J. Geophys. Res. Atmos.*, **121**, 2593–2609, doi:[10.1002/2015JD024525](https://doi.org/10.1002/2015JD024525).
- Klein, S. A., and C. Jakob, 1999: Validation and sensitivities of frontal clouds simulated by the ECMWF model. *Mon. Wea. Rev.*, **127**, 2514–2531, doi:[10.1175/1520-0493\(1999\)127<2514:VASOFC>2.0.CO;2](https://doi.org/10.1175/1520-0493(1999)127<2514:VASOFC>2.0.CO;2).
- , and A. Hall, 2015: Emergent constraints for cloud feedbacks. *Curr. Climate Change Rep.*, **1**, 276–287, doi:[10.1007/s40641-015-0027-1](https://doi.org/10.1007/s40641-015-0027-1).
- Klocke, D., R. Pincus, and J. Quaas, 2011: On constraining estimates of climate sensitivity with present-day observations through model weighting. *J. Climate*, **24**, 6092–6099, doi:[10.1175/2011JCLI4193.1](https://doi.org/10.1175/2011JCLI4193.1).
- Knutti, R., and G. C. Hegerl, 2008: The equilibrium sensitivity of the Earth's temperature to radiation changes. *Nat. Geosci.*, **1**, 735–743, doi:[10.1038/ngeo337](https://doi.org/10.1038/ngeo337).
- , D. Masson, and A. Gottelman, 2013: Climate model genealogy: Generation CMIP5 and how we got there. *Geophys. Res. Lett.*, **40**, 1194–1199, doi:[10.1002/grl.50256](https://doi.org/10.1002/grl.50256).
- Le Treut, H., and Z. X. Li, 1991: Sensitivity of an atmospheric general circulation model to prescribed SST changes: Feedback effects associated with the simulation of cloud optical properties. *Climate Dyn.*, **5**, 175–187, doi:[10.1007/BF00251808](https://doi.org/10.1007/BF00251808).
- Maslin, M., and P. Austin, 2012: Uncertainty: Climate models at their limit? *Nature*, **486**, 183–184, doi:[10.1038/486183a](https://doi.org/10.1038/486183a).
- McKay, M. D., R. J. Beckman, and W. J. Conover, 1979: A comparison of three methods for selecting values of input variables in the analysis of output from a computer code. *Technometrics*, **21**, 239–245.
- Mellor, G. L., and T. Yamada, 1974: A hierarchy of turbulence closure models for planetary boundary layers. *J. Atmos. Sci.*, **31**, 1791–1806, doi:[10.1175/1520-0469\(1974\)031<1791:AHOTCM>2.0.CO;2](https://doi.org/10.1175/1520-0469(1974)031<1791:AHOTCM>2.0.CO;2).

- , and —, 1982: Development of a turbulence closure model for geophysical fluid problems. *Rev. Geophys.*, **20**, 851–875, doi:[10.1029/RG020i004p00851](https://doi.org/10.1029/RG020i004p00851).
- Murphy, J., D. M. H. Sexton, D. N. Barnett, G. S. Jones, M. J. Webb, M. Collins, and D. A. Stainforth, 2004: Quantification of modelling uncertainties in a large ensemble of climate change simulations. *Nature*, **430**, 768–772, doi:[10.1038/nature02771](https://doi.org/10.1038/nature02771).
- Nakanishi, M., 2001: Improvement of the Mellor–Yamada turbulence closure model based on large-eddy simulation data. *Bound.-Layer Meteor.*, **99**, 349–378, doi:[10.1023/A:1018915827400](https://doi.org/10.1023/A:1018915827400).
- , and H. Niino, 2004: An improved Mellor–Yamada level-3 model with condensation physics: Its design and verification. *Bound.-Layer Meteor.*, **112**, 1–31, doi:[10.1023/B:BOUN.0000020164.04146.98](https://doi.org/10.1023/B:BOUN.0000020164.04146.98).
- Ogura, T., S. Emori, M. J. Webb, Y. Tsushima, T. Yokohata, A. Abe-Ouchi, and M. Kimoto, 2008: Towards understanding cloud response in atmospheric GCMs: The use of tendency diagnostics. *J. Meteor. Soc. Japan*, **86**, 69–79, doi:[10.2151/jmsj.86.69](https://doi.org/10.2151/jmsj.86.69).
- Pan, D. M., and D. A. Randall, 1998: A cumulus parameterization with a prognostic closure. *Quart. J. Roy. Meteor. Soc.*, **124**, 949–981, doi:[10.1002/qj.49712454714](https://doi.org/10.1002/qj.49712454714).
- Piani, C., D. J. Frame, D. A. Stainforth, and M. R. Allen, 2005: Constraints on climate change from a multi-thousand member ensemble of simulations. *Geophys. Res. Lett.*, **32**, L23825, doi:[10.1029/2005GL024452](https://doi.org/10.1029/2005GL024452).
- Pincus, R., S. Platnick, S. A. Ackerman, R. S. Hemler, and R. J. P. Hofmann, 2012: Reconciling simulated and observed views of clouds: MODIS, ISCCP, and the limits of instrument simulators. *J. Climate*, **25**, 4699–4720, doi:[10.1175/JCLI-D-11-00267.1](https://doi.org/10.1175/JCLI-D-11-00267.1).
- Qu, X., A. Hall, S. A. Klein, and P. M. Caldwell, 2014: On the spread of changes in marine low cloud cover in climate model simulations of the 21st century. *Climate Dyn.*, **42**, 2603–2626, doi:[10.1007/s00382-013-1945-z](https://doi.org/10.1007/s00382-013-1945-z).
- Reichler, T., and J. Kim, 2008: How well do coupled models simulate today's climate? *Bull. Amer. Meteor. Soc.*, **89**, 303–311, doi:[10.1175/BAMS-89-3-303](https://doi.org/10.1175/BAMS-89-3-303).
- Rienecker, M. M., and Coauthors, 2011: MERRA: NASA's Modern-Era Retrospective Analysis for Research and Applications. *J. Climate*, **24**, 3624–3648, doi:[10.1175/JCLI-D-11-00015.1](https://doi.org/10.1175/JCLI-D-11-00015.1).
- Sanderson, B. M., 2011: A multimodel study of parametric uncertainty in predictions of climate response to rising greenhouse gas concentrations. *J. Climate*, **24**, 1362–1377, doi:[10.1175/2010JCLI3498.1](https://doi.org/10.1175/2010JCLI3498.1).
- , K. M. Shell, and W. Ingram, 2010: Climate feedbacks determined using radiative kernels in a multithousand member ensemble of AOGCMs. *Climate Dyn.*, **35**, 1219–1236, doi:[10.1007/s00382-009-0661-1](https://doi.org/10.1007/s00382-009-0661-1).
- Sherwood, S. C., C. L. Meyer, R. J. Allen, and H. A. Titchner, 2008: Robust tropospheric warming revealed by iteratively homogenized radiosonde data. *J. Climate*, **21**, 5336–5352, doi:[10.1175/2008JCLI2320.1](https://doi.org/10.1175/2008JCLI2320.1).
- , S. Bony, and J.-L. Dufresne, 2014: Spread in model climate sensitivity traced to atmospheric convective mixing. *Nature*, **505**, 37–42, doi:[10.1038/nature12829](https://doi.org/10.1038/nature12829).
- Shiogama, M., and Coauthors, 2012: Perturbed physics ensemble using the MIROC5 coupled atmosphere–ocean GCM without flux corrections: Experimental design and results. *Climate Dyn.*, **39**, 3041–3056, doi:[10.1007/s00382-012-1441-x](https://doi.org/10.1007/s00382-012-1441-x).
- , M. Watanabe, T. Ogura, T. Yokohata, and M. Kimoto, 2014: Multi-parameter multi-physics ensemble (MPMPE): A new approach exploring the uncertainties of climate sensitivity. *Atmos. Sci. Lett.*, **15**, 97–102, doi:[10.1002/asl2.472](https://doi.org/10.1002/asl2.472).
- Soden, B. J., I. M. Held, R. Colman, K. M. Shell, J. T. Kiehl, and C. A. Shields, 2008: Quantifying climate feedbacks using radiative kernels. *J. Climate*, **21**, 3504–3520, doi:[10.1175/2007JCLI2110.1](https://doi.org/10.1175/2007JCLI2110.1).
- Stainforth, D. A., and Coauthors, 2005: Uncertainty in predictions of the climate response to rising levels of greenhouse gases. *Nature*, **433**, 403–406, doi:[10.1038/nature03301](https://doi.org/10.1038/nature03301).
- Taylor, K. E., R. J. Stouffer, and G. A. Meehl, 2012: An overview of CMIP5 and the experiment design. *Bull. Amer. Meteor. Soc.*, **93**, 485–498, doi:[10.1175/BAMS-D-11-00094.1](https://doi.org/10.1175/BAMS-D-11-00094.1).
- Tebaldi, C., and R. Knutti, 2007: The use of the multi-model ensemble in probabilistic climate projections. *Philos. Trans. Roy. Soc. London*, **365A**, 2053–2075, doi:[10.1098/rsta.2007.2076](https://doi.org/10.1098/rsta.2007.2076).
- Tomassini, L., A. Voigt, and B. Stevens, 2015: On the connection between tropical circulation, convective mixing, and climate sensitivity. *Quart. J. Roy. Meteor. Soc.*, **141**, 1404–1416, doi:[10.1002/qj.2450](https://doi.org/10.1002/qj.2450).
- Tsushima, Y., and Coauthors, 2006: Importance of the mixed-phase cloud distribution in the control climate for assessing the response of clouds to carbon dioxide increase: A multi-model study. *Climate Dyn.*, **27**, 113–126, doi:[10.1007/s00382-006-0127-7](https://doi.org/10.1007/s00382-006-0127-7).
- Vial, J., J.-L. Dufresne, and S. Bony, 2013: On the interpretation of inter-model spread in CMIP5 climate sensitivity estimates. *Climate Dyn.*, **41**, 3339–3362, doi:[10.1007/s00382-013-1725-9](https://doi.org/10.1007/s00382-013-1725-9).
- Watanabe, M., S. Emori, M. Satoh, and H. Miura, 2009: A PDF-based hybrid prognostic cloud scheme for general circulation models. *Climate Dyn.*, **33**, 795–816, doi:[10.1007/s00382-008-0489-0](https://doi.org/10.1007/s00382-008-0489-0).
- , and Coauthors, 2010: Improved climate simulation by MIROC5: Mean states, variability, and climate sensitivity. *J. Climate*, **23**, 6312–6335, doi:[10.1175/2010JCLI3679.1](https://doi.org/10.1175/2010JCLI3679.1).
- , and Coauthors, 2012: Using a multi-physics ensemble for exploring diversity in cloud-shortwave feedback in GCMs. *J. Climate*, **25**, 5416–5431, doi:[10.1175/JCLI-D-11-00564.1](https://doi.org/10.1175/JCLI-D-11-00564.1).
- Webb, M., C. Senior, S. Bony, and J. J. Morcrette, 2001: Combining ERBE and ISCCP data to assess clouds in the Hadley Centre, ECMWF and LMD atmospheric climate models. *Climate Dyn.*, **17**, 905–922, doi:[10.1007/s003820100157](https://doi.org/10.1007/s003820100157).
- , and Coauthors, 2006: On the contribution of local feedback mechanisms to the range of climate sensitivity in two GCM ensembles. *Climate Dyn.*, **27**, 17–38, doi:[10.1007/s00382-006-0111-2](https://doi.org/10.1007/s00382-006-0111-2).
- , F. Lambert, and J. Gregory, 2013: Origins of differences in climate sensitivity, forcing and feedback in climate models. *Climate Dyn.*, **40**, 677–707, doi:[10.1007/s00382-012-1336-x](https://doi.org/10.1007/s00382-012-1336-x).
- Wilson, D. R., and S. P. Ballard, 1999: A microphysically based precipitation scheme for the UK Meteorological Office Unified Model. *Quart. J. Roy. Meteor. Soc.*, **125**, 1607–1636, doi:[10.1002/qj.49712555707](https://doi.org/10.1002/qj.49712555707).
- Yamazaki, K., and Coauthors, 2013: Obtaining diverse behaviors in a climate model without the use of flux adjustments. *J. Geophys. Res. Atmos.*, **118**, 2781–2793, doi:[10.1002/jgrd.50304](https://doi.org/10.1002/jgrd.50304).
- Yokohata, T., M. J. Webb, M. Collins, K. D. Williams, M. Yoshimori, J. C. Hargreaves, and J. D. Annan, 2010: Structural similarities and differences in climate responses to CO₂ increase between two perturbed physics ensembles. *J. Climate*, **23**, 1392–1410, doi:[10.1175/2009JCLI2917.1](https://doi.org/10.1175/2009JCLI2917.1).
- , and Coauthors, 2013: Reliability and importance of structural diversity of climate model ensembles. *Climate Dyn.*, **41**, 2745–2763, doi:[10.1007/s00382-013-1733-9](https://doi.org/10.1007/s00382-013-1733-9).

- Zelinka, M. D., S. A. Klein, and D. L. Hartmann, 2012a: Computing and partitioning cloud feedbacks using cloud property histograms. Part I: Cloud radiative kernels. *J. Climate*, **25**, 3715–3735, doi:[10.1175/JCLI-D-11-00248.1](https://doi.org/10.1175/JCLI-D-11-00248.1).
- , —, and —, 2012b: Computing and partitioning cloud feedbacks using cloud property histograms. Part II: Attribution to changes in cloud amount, altitude, and optical depth. *J. Climate*, **25**, 3736–3754, doi:[10.1175/JCLI-D-11-00249.1](https://doi.org/10.1175/JCLI-D-11-00249.1).
- , —, K. Taylor, T. Andrews, M. Webb, J. Gregory, and P. Forster, 2013: Contributions of different cloud types to feedbacks and rapid adjustments in CMIP5. *J. Climate*, **26**, 5007–5027, doi:[10.1175/JCLI-D-12-00555.1](https://doi.org/10.1175/JCLI-D-12-00555.1).
- Zhang, M., and Coauthors, 2013: CGILS: Results from the first phase of an international project to understand the physical mechanisms of low cloud feedbacks in single column models. *J. Adv. Model. Earth Syst.*, **5**, 826–842, doi:[10.1002/2013MS000246](https://doi.org/10.1002/2013MS000246).
- Zhao, M., 2014: An investigation of the connections among convection, clouds, and climate sensitivity in a global climate model. *J. Climate*, **27**, 1845–1862, doi:[10.1175/JCLI-D-13-00145.1](https://doi.org/10.1175/JCLI-D-13-00145.1).